Impact of thermal management and ambient temperature on aging of LFP, NMC, and NCA batteries for EVs

Elena-Daniela Lupu*[1,2], *Ștefan Lucian* Tabacu[2], *Elena-Crenguța* Bobric[1], *Daniela* Irimia[1], and *Valentin* Vlad[1]
[1] Ștefan cel Mare University of Suceava, 13 Universității Street, 720229 Suceava, Romania
[2] National University of Science and Technology Politehnica Bucharest, University Centre of Pitești, 110040, Romania

Abstract. This paper presents a comparative electro-thermal and aging-aware analysis of lithium-ion batteries with LFP, NMC and NCA chemistries for electric vehicle applications. A unified vehicle–battery modelling framework is developed based on a longitudinal vehicle dynamics model, an equivalent circuit battery model with temperature-dependent parameters, and a lumped thermal model including heat generation and dissipation mechanisms. Battery aging is described through a temperature-dependent degradation formulation linked to electrochemical activation processes. A PI-based supervisory TMS controller is implemented to regulate battery temperature while minimizing auxiliary energy demand. Equal nominal pack energy is enforced across all chemistries. Simulations are performed under four ambient temperatures (–10 °C, 0 °C, 25 °C, and 40 °C) and representative driving cycles. The results demonstrate significant differences among the considered chemistries in terms of peak temperature, energy losses, and estimated capacity fade, and reveal the strong influence of ambient temperature and thermal management on degradation rate. A sensitivity analysis further identifies internal resistance and heat transfer capability as dominant factors affecting thermal and aging behavior. The proposed framework enables a quantitative and physics-consistent comparison of lithium-ion battery chemistries and supports the design of thermal management strategies for electric vehicles.

1 Introduction

Battery electric vehicles (BEVs) represent the dominant solution for road transport electrification, relying on lithium-ion batteries as on-board energy storage systems. Battery-electric vehicles rely on lithium-ion packs whose efficiency, power capability, and lifetime are strongly temperature-dependent. Low ambient temperatures increase internal resistance and reduce power/efficiency, while elevated temperatures accelerate degradation and raise safety constraint [1-3].

Among the dominant EV chemistries, lithium iron phosphate (LFP) provides high thermal stability and long cycle life at the expense of lower specific energy, whereas lithium nickel manganese cobalt oxide (NMC) and lithium nickel cobalt aluminium oxide (NCA) offer higher energy density but typically exhibit stronger temperature sensitivity and accelerated aging under high-temperature operation [1], [3], [4]. These chemistry-dependent differences influence degradation pathways, thermal behavior, and safety margins, including the onset conditions for thermal runaway [5].

Although numerous studies address thermal management and battery aging, cross-chemistry comparisons are often performed under non-unified assumptions (different pack sizing, load profiles, or thermal control), which limits quantitative fairness at vehicle level [3], [6-8].

Extensive research has addressed battery thermal management systems (TMS), demonstrating that active cooling reduces peak temperature and improves safety margins. However, several works emphasize thermal metrics without fully quantifying the coupled electro-thermal degradation effects under realistic driving profiles [6-11].

This study proposes an integrated vehicle-to-battery electro-thermal and aging-aware simulation framework that couples longitudinal vehicle dynamics, drivetrain efficiency (motor maps and inverter losses), a temperature-dependent 1RC battery ECM, a PI-based TMS (cooling/heating with auxiliary power accounting), and a semi-empirical aging law. Equal nominal pack energy is enforced across all chemistries under Artemis Urban and Artemis130 cycles at −10 °C, 0 °C, 25 °C, and 40 °C. The vehicle model, driving cycles, nominal pack energy, SoC operating window, and TMS control strategy are kept identical, while chemistry-dependent differences are introduced only through the OCV and ECM parameter maps, power/current derating limits, and thermal and aging parameters. This integrated approach responds to the need identified in recent literature for coupled electro-thermal-aging modelling frameworks capable of linking vehicle-level operation with battery lifetime prediction.

* Corresponding author: elena.lupu@usm.ro

2 Integrated electro-thermal and aging modelling framework

An integrated vehicle-to-battery electro-thermal and aging-aware simulation framework is developed to evaluate lithium-ion battery performance and degradation under transient driving conditions, consistent with contemporary modelling approaches combining ECM, thermal, and SoH prediction layers [3], [12].

The overall modelling workflow is shown in Figure 1. The prescribed driving cycle is converted into traction power through the vehicle dynamics model and propagated through drivetrain efficiency maps, the battery ECM, the thermal model, and the aging module. Simulations are performed for LFP, NMC, and NCA chemistries under Artemis Urban and Artemis130 cycles at four ambient temperatures.

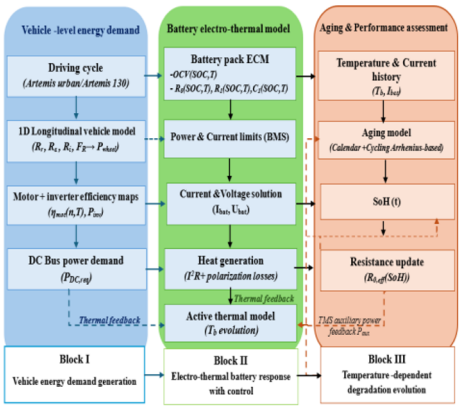

Fig. 1. Workflow of energy simulation

2.1 Longitudinal vehicle model

The longitudinal vehicle dynamics are described by a quasi-static model that converts the prescribed speed profile into traction force and power demand considering rolling resistance, aerodynamic drag, grade resistance and inertial effects. Motion is considered only along the driving direction, with resistive and inertial forces computed from the prescribed speed profile $v(t)$ and its time derivative $a(t)$.

The total resistive force at the wheel is expressed as:

$$F_R = f_r \cdot m \cdot g + \frac{1}{2} \cdot \rho \cdot c_x \cdot A \cdot v^2 + m \cdot g \cdot \sin(\alpha) + m \cdot \delta \cdot a \quad (1)$$

Here, m is the vehicle mass, f_r the rolling resistance coefficient, c_x the aerodynamic drag coefficient, A the frontal area, ρ the air density, v the vehicle speed, a the longitudinal acceleration, and δ the equivalent rotational inertia factor.

The mechanical power at the wheel is given by:

$$P_w = F_R \cdot v \quad (2)$$

Although suitable for traction power and energy estimation under prescribed driving cycles, this quasi-static formulation neglects three-dimensional aerodynamic effects, load transfer, tire slip, and detailed drivetrain dynamics.

Simulations are conducted for a C-segment compact BEV representative of current mid-size passenger vehicles. The main parameters are: $m = 1950$ kg, $c_x = 0.26$, $A = 2.36\,\mathrm{m}^2$, $f_r = 0.011$, wheel radius $r_r = 0.351$m, fixed transmission ratio $i_{tr} = 7$, and mechanical efficiency $\eta_{tr} = 0.95$.

Figure 2 presents the longitudinal vehicle dynamics model and the corresponding traction power calculation chain, linking the prescribed speed profile to wheel force and mechanical power demand.

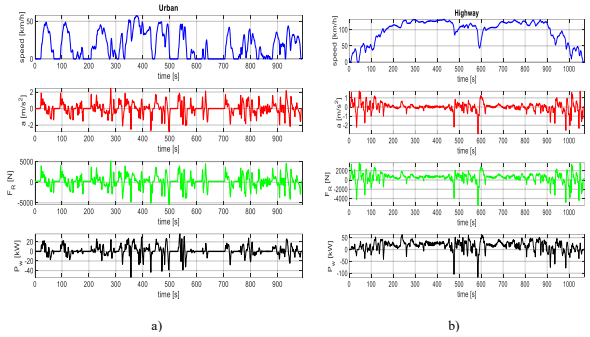

Fig. 2. Longitudinal vehicle dynamics and traction power: a) for Artemis Urban driving cycles, b) Artemis130 driving cycles.

2.2 Drivetrain, motor and inverter modelling

The drivetrain is modelled using a fixed transmission ratio i_{tr} and constant mechanical transmission efficiency η_{tr}. Wheel torque and speed are mapped to motor torque and speed through:

$$\omega_m = i_{tr}\,\omega_w, \qquad T_m = \begin{cases} \frac{T_w}{i_{tr}\eta_{tr}}, & T_w \geq 0 \\ \frac{T_w \eta_{tr}}{i_{tr}}, & T_w < 0 \end{cases} \quad (3)$$

where positive torque corresponds to traction and negative torque to regenerative operation.

Motor efficiency is obtained from two-dimensional lookup tables $\eta_m = \eta(n_m, T_m)$derived from finite element (FEM) electromagnetic simulations of an interior permanent magnet synchronous machine (IPMSM) with V-shaped rotor configuration. At each step, the operating points defined by the driving cycle are projected onto the efficiency map to determine instantaneous motor efficiency (Figure 3).

The operating points mapped onto the motor efficiency diagram confirm that both cycles cover broad regions of the torque–speed domain, including medium-efficiency and high-efficiency zones, as well as partial-load regions. This validates that the selected cycles are suitable for stressing both drivetrain efficiency and battery electro-thermal behavior under realistic operating conditions.

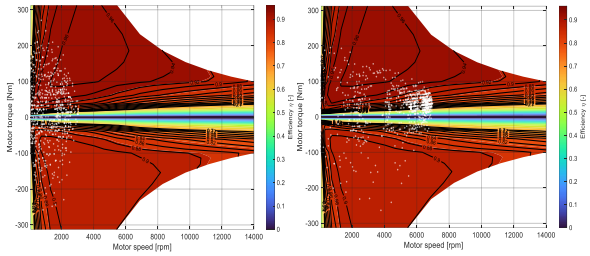

Fig. 3. Distribution of motor operating points over the FEM-based efficiency map for Artemis Urban and Artemis130 driving cycles

Phase current is obtained from dedicated lookup tables and converted to line current. Inverter losses are modeled after sum of quadratic conduction and frequency-dependent switching components:

$$P_{inv} = k_{cond} I^2 + k_{sw} f_e \tag{4}$$

where f_e denotes the electrical frequency.

In regenerative mode, generator efficiency is adjusted by a speed- and torque-dependent correction factor: $\eta_{gen} = k_{gen}(n_m, T_m)\eta_m$.

The resulting DC bus requested power is computed separately for traction and regenerative modes:

- traction:

$$P_{dc,req} = \frac{P_{mech}}{\eta_m} + P_{inv} \tag{5}$$

- regeneration:

$$P_{dc,req} = P_{mech}\, \eta_{gen}\, \eta_{regen,sys} + P_{inv} \tag{6}$$

2.3 Battery electrical model

The battery pack is modeled using a temperature-dependent first-order Thevenin equivalent circuit (1RC ECM), consisting of an open-circuit voltage source U_{oc}, an ohmic resistance R_0, and a single RC polarization branch. This modelling approach is widely adopted in EV battery simulations due to its balance between computational efficiency and accuracy [3], [4], [12].

Cell-level parameters are implemented as two-dimensional lookup tables dependent on state of charge and temperature:

$$\begin{aligned} U_{oc} &= U_{oc}(SoC, T) \\ R_0 &= R_0(SoC, T) \\ R_1 &= R_1(SoC, T),\ \ C_1 = C_1(SoC, T) \end{aligned} \tag{7}$$

Pack-level parameters are obtained through series–parallel scaling of the cell quantities:

$$R_{0,pack} = \frac{N_s}{N_p} R_0\ ,\ R_{1,pack} = \frac{N_s}{N_p} R_1 \qquad C_{1,pack} = \frac{N_p}{N_s} C_1 \tag{8}$$

where N_s and N_p denote the number of series- and parallel-connected cells, respectively.

The pack open-circuit voltage scales linearly with the number of series-connected cells:

$$U_{oc,pack}(SoC, T) = N_s \cdot U_{oc,cell}(SoC, T) \tag{9}$$

The terminal voltage of the battery pack is given as:

$$U_{bat} = U_{oc,pack} - I R_{0,pack} - U_1 \tag{10}$$

with polarization voltage dynamics:

$$\frac{dU_1}{dt} = -\frac{U_1}{R_{1,pack} C_{1,pack}} + \frac{I}{C_{1,pack}} \tag{11}$$

Battery current is computed at each time from the nonlinear power balance:

$$P = U_{bat} \cdot I \tag{12}$$

subject to SoC- and temperature-dependent current and power derating limits enforced by the battery management system (BMS).

The OCV–SoC relationship is chemistry-dependent. LFP exhibits a pronounced mid-SoC voltage plateau with reduced voltage sensitivity, whereas NMC and NCA show a more monotonic increase over the usable SoC range, affecting SoC observability and estimation robustness [3].

Table 1. Cell-Level Performance Characteristics of Considered Lithium-Ion Chemistries

Parameter	LFP ($LiFePO_4$)	NMC ($LiNi_xMn_yCo\_zO_2$)	NCA ($LiNiCo\ AlO_2$)
Specific energy [Wh/kg]	150–170	180–260	200–300
Cycle life (to 80% SoH)	3000–6000	1000–2000	1000–1500
Thermal runaway onset [°C]	> 250	~210–230	~200–220
Nominal cell voltage [V]	~3.2–3.3	~3.6	~3.6–3.7

Table 1 summarizes representative electrochemical and thermal characteristics of the considered lithium-ion chemistries, consistent with state-of-the-art comparative assessments of EV battery technologies [1], [3-5].

A uniform nominal pack energy of 100 kWh is imposed across all chemistries for fair comparison. Assuming 50 Ah traction-grade cells and a 400 V class architecture, the resulting configurations are 125s5p for LFP and 108s5p for NMC and NCA (≈400 V, ≈250 Ah).

2.4 Thermal model and heat generation

A lumped thermal model is adopted to represent the battery pack with a single bulk temperature state and effective thermal parameters. This formulation is widely used in vehicle-level electro-thermal simulations due to its balance between computational efficiency and predictive capability for pack-average temperature evolution under driving cycles. The approach neglects

spatial temperature gradients and localized hot spots, but previous studies report typical prediction differences of about 1–3 °C compared with multi-node models under moderate driving loads. Therefore, it is suitable for the present comparative analysis. [2], [6], [10].

Heat generation is assumed to originate from ohmic and polarization losses within the equivalent circuit model:

$$Q_{gen} = I^2 R_{0,pack} + \frac{U_1^2}{R_{1,pack}} \quad (13)$$

The temperature dynamics follow:

$$C_{th}\frac{dT_b}{dt} = Q_{gen} + Q_{heat} - Q_{cool} - \frac{T_b - T_{amb}}{R_{th}} \quad (14)$$

The strong coupling between temperature evolution and degradation rate is extensively documented in experimental and modelling studies, which show exponential temperature dependence of aging mechanisms [1], [2], [3].

2.5 Thermal management system

An active thermal management controller regulates battery temperature around a reference setpoint. Cooling is governed by a proportional–integral (PI) controller with a temperature deadband, while heating is activated below a predefined threshold.

Active and passive thermal management strategies, and their influence on aging and safety margins, have been comparatively analyzed in recent literature

Studies demonstrate that inadequate thermal control accelerates capacity fade and may reduce thermal runaway thresholds in aged cells

The total auxiliary power consumption is added to the DC bus battery power request:

$$P_{req} = P_{dc,req} + P_{aux} \quad (15)$$

ensuring energetic consistency between thermal control actions and battery electrical loading.

2.6 Aging and state-of-health model

Battery degradation is modelled using a temperature- and current-dependent semi-empirical formulation combining calendar and cycling contributions, consistent with widely adopted lifetime modelling frameworks [3].

The exponential temperature dependence reflects Arrhenius-type activation behavior of dominant degradation mechanisms such as SEI growth and lithium loss, as documented in aging reviews [2], [3].

The incremental SoH reduction at each time step is expressed as:

$$\Delta SoH = k_{cal}\exp\left(-\frac{E_{a,cal}}{RT}\right)(\Delta t)^{\alpha} + k_{cyc}\exp\left(-\frac{E_{a,cyc}}{RT}\right)\left(\frac{|I|}{I_{ref}}\right)^{\beta}\Delta t \quad (16)$$

The aging model coefficients (k_{cal}, k_{cyc}, $E_{a,cal}$, $E_{a,cyc}$, α, β) are selected from parameter ranges reported in lithium-ion aging studies and calibrated to reproduce representative degradation trends for automotive-grade LFP, NMC and NCA cells at reference conditions (≈25 °C and moderate current levels corresponding to ~0.5–1C cycling). Chemistry-dependent differences are introduced mainly through the cycling degradation coefficient and activation energy, reflecting the higher temperature sensitivity of nickel-rich chemistries compared with LFP. A ±20% variation of degradation coefficients results in proportional changes in capacity fade while preserving the relative degradation ranking between chemistries, indicating that the comparative conclusions are robust to moderate parameter uncertainty.

Long-term SoH evolution is obtained by mapping transient current throughput to equivalent full cycles (EFC), consistent with practical RUL estimation methodologies applied in EV-oriented battery prognostics.

2.7 Modelling assumptions and limitations

The framework targets system-level comparative assessment rather than high-fidelity electrochemical resolution. The 1RC ECM and lumped thermal approach represent a trade-off between computational efficiency and physical detail, aligned with modelling hierarchies described in comprehensive reviews [3], [4].

The aging model is semi-empirical and calibrated at reference conditions, without explicitly resolving SEI growth or lithium plating. Despite these simplifications, the model preserves the dominant couplings between load profile, temperature, thermal management, and degradation, enabling consistent cross-chemistry and cross-temperature comparisons under realistic driving cycles. Future work may extend the framework toward spatially resolved thermal models or electrochemical-thermal formulations in order to capture intra-pack gradients and localized aging phenomena

3 Electro-thermal performance and aging comparison under varying ambient conditions

To ensure a realistic and application-oriented comparison, an application-driven sizing scenario is adopted in which the battery pack is dimensioned for a 350 km target range. The nominal energy is derived from the worst-case specific consumption across the considered cycles, assuming 80% usable depth-of-discharge (DoD) and a 20% design margin and is imposed identically for all chemistries to ensure fair comparison.

The analysis is conducted under the Artemis Urban (≈4.87 km) and Artemis130 (≈28.7 km) cycles, which impose fundamentally different load patterns. The urban cycle is characterized by frequent transient and regenerative events, whereas the highway cycle

involves sustained high-speed aerodynamic loading. Consequently, the highway scenario exhibits a substantially higher net DC bus energy demand (6.55 kWh) compared to the urban cycle (0.80 kWh), as shown in Figure 4.

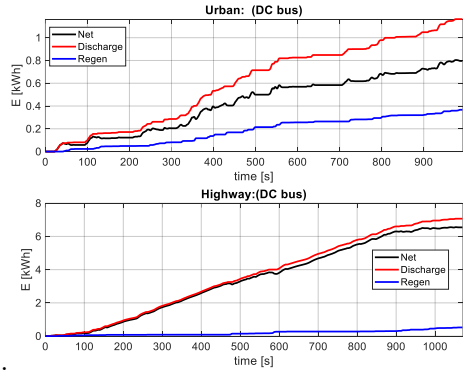

.

Fig. 4. Cumulative energy (Net, Discharge, Regen)

The corresponding specific energy consumption (Figure 5) increases from 163.4 Wh/km in urban operation to 227.8 Wh/km under highway conditions, confirming the dominant influence of aerodynamic drag at sustained speeds.

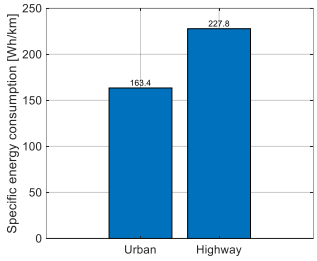

Fig. 5. Specific energy consumption (Wh/km) for Artemis Urban and Artemis130 driving cycles

Figures 4–5 quantify the cycle energy and specific consumption at the DC bus, accounting for drivetrain conversion losses (motor efficiency maps and inverter losses) and regenerative efficiency. To include battery internal losses and the thermal-management demand, the energy balance is additionally evaluated at the battery terminals using $P_{bat}(t)$, where $P_{bat}(t)$supplies both traction power and the TMS auxiliary load $P_{aux}(t)$.

Figure 6 summarizes, for all chemistries and ambient conditions, the net battery-terminal energy $E_{net,bat}$and thermal auxiliary energy E_{aux}. The auxiliary demand is highest at subzero ambient temperatures due to pack heating, becomes negligible around 25 °C, and remains modest at 40 °C, where cooling is only intermittently activated over the relatively short driving cycles.

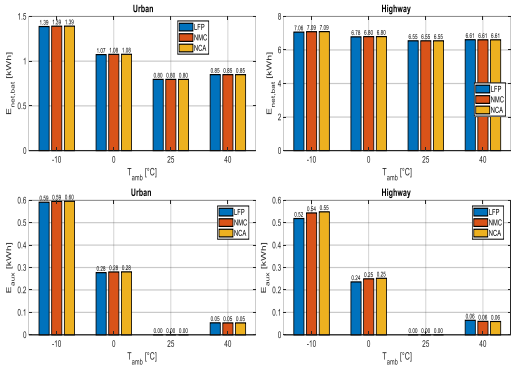

Fig. 6. Battery-terminal energy balance ($E_{net,bat}$ and E_{aux})

Figure 7 presents the peak temperature rise above ambient ($\Delta T_{peak} = T_{peak} - T_{amb}$) for LFP, NMC, and NCA under Urban and Highway cycles. ΔT_{peak} decreases with increasing ambient temperature, reflecting the reduction of internal resistance and heat generation at higher temperatures. At −10 °C and 0 °C, the temperature rise reaches 10–20 °C due to elevated ohmic losses, with LFP exhibiting slightly higher ΔT_{peak} consistent with its higher low-temperature resistance. At 25 °C, ΔT_{peak} becomes marginal (<2 °C), while at 40 °C it is nearly negligible.

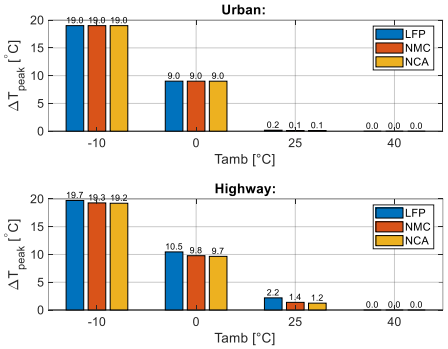

Fig. 7. Peak Battery Pack Temperature Rise (ΔT_{peak}) Relative to Ambient**.**

However, low ΔT_{peak} at high ambient temperature does not imply reduced thermal stress, since the absolute operating temperature remains elevated and accelerates aging.

Figure 8 illustrates the electro-thermal response under the most demanding highway condition at 40 °C. Although the load profile is identical, chemistry-dependent voltage levels and internal losses lead to different loss amplitudes and auxiliary activation patterns. The TMS effectively limits battery temperature close to the control setpoint, ensuring comparable thermal conditions for subsequent aging comparison.

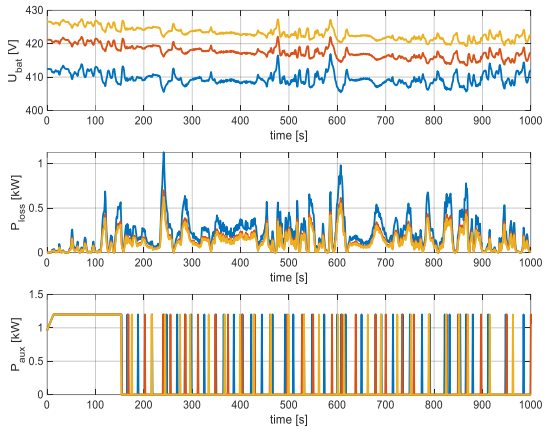

Fig. 8. Battery voltage, internal losses and TMS auxiliary power during Highway cycle at 40 °C (initial SoC = 80%)

Figure 9 shows relative capacity fade versus Equivalent Full Cycles for the three chemistries at four ambient temperatures. Degradation increases with temperature; LFP exhibits the lowest fade and longest lifetime (20% EOL criterion), followed by NMC, while NCA shows the shortest lifetime under identical conditions.

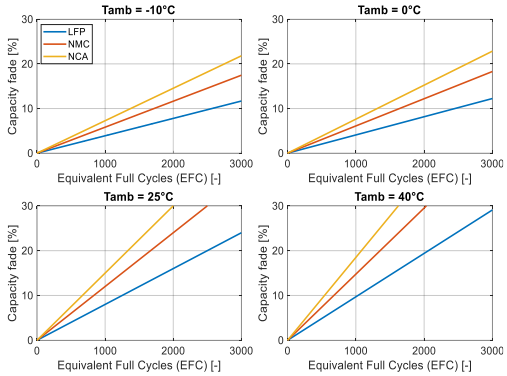

Fig. 9. Temperature-Dependent Capacity Fade vs. EFC

Figure 10 shows SoC- and temperature-dependent pack-level ECM parameters for LFP, NMC, and NCA. Both ohmic and polarization resistances increase at low temperatures, raising internal losses and heat generation. LFP exhibits higher absolute resistance, whereas NMC and NCA display lower nominal resistance but stronger temperature sensitivity.

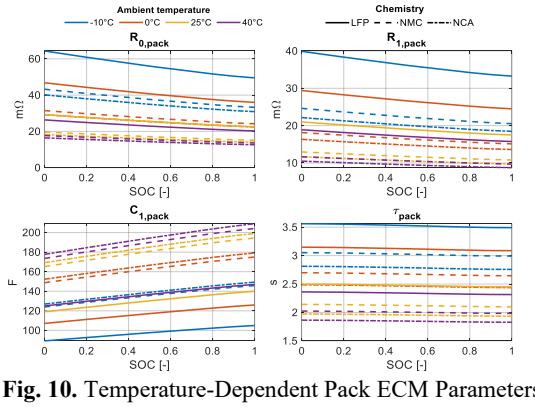

Fig. 10. Temperature-Dependent Pack ECM Parameters vs SoC

These parameter variations govern electrical losses and thermal response, thereby shaping the chemistry-dependent degradation trajectories discussed subsequently.

To quantify the effect of ambient temperature, a relative sensitivity index is defined with respect to the reference condition at 25 °C:

$$S(T) = \frac{X(T) - X_{25°C}}{X_{25°C}} \times 100\% \quad (17)$$

where X denotes the cumulative capacity fade over the considered driving profile.

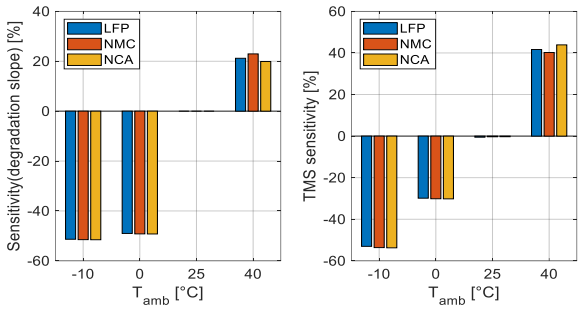

Fig. 11. Relative Capacity Fade Sensitivity to Ambient Temperature

Figure 11 shows a pronounced non-linear dependence of degradation on ambient temperature. For all chemistries, minimum degradation occurs around 25 °C, while both subzero and elevated temperatures increase capacity fade. At −10 °C, degradation rises mainly due to increased internal resistance and associated losses. In contrast, at 40 °C, degradation acceleration is driven by temperature-dependent electrochemical kinetics described by the Arrhenius-type aging formulation.

4 Conclusion

Capacity fade versus EFC reveals strong temperature dependence across all chemistries. Degradation is most severe at 40 °C and minimal around 25 °C. LFP shows the lowest fade and weakest temperature sensitivity, followed by NMC, while NCA is most susceptible, particularly at elevated temperatures, emphasizing the importance of thermal management for nickel-rich chemistries.

Under identical ambient conditions, the highway cycle accelerates aging compared to the urban cycle due to sustained positive power demand, higher average current, and increased thermal stress, whereas intermittent loading and regeneration in urban driving reduce cumulative damage.

Lifetime divergence is mainly driven by chemistry-specific ECM parameters governing resistance and heat generation under identical loads. A temperature sensitivity index (referenced to 25 °C) further indicates that degradation rate is the most temperature-sensitive metric, followed by auxiliary energy demand, while DC-bus traction energy shows comparatively lower sensitivity.

References

1. S. Serarslan, The impact of temperature and ageing on LFP electric vehicle batteries: A comprehensive modelling study. Int. J. Automot. Sci. Technol. **9**, 12–25 (2025). https://doi.org/10.30939/ijastech..1519778
2. L. Spitthoff, P. R. Shearing, O. S. Burheim, Temperature, ageing and thermal management of lithium-ion batteries. Energies **14**, 1248 (2021). https://doi.org/10.3390/en14051248
3. W. Vermeer, G. R. Chandra et al. A comprehensive review on the characteristics and modeling of lithium-ion battery aging. IEEE Trans. Transp. Electr. **8**, 2205–2232 (2022). https://doi.org/10.1109/TTE.2021.3138357
4. R. R. Kumar, C. Bharatiraja, et al. Advances in batteries, battery modeling, battery management system, battery thermal management, SoC, SoH, and charge/discharge characteristics in EV applications. IEEE Access **11**, 105761–105809 (2023). https://doi.org/10.1109/ACCESS.2023.3318121
5. J. Wang, Y. Chen, Y. Mei, K. Lu, Influence of aging on thermal runaway behavior of lithium-ion batteries: Experiments and simulations for engineering education. Fire **8**, 479 (2025). https://doi.org/10.3390/fire8120479
6. N. Nagaraju Napa, M. K. Agrawal Impact of active and passive thermal management strategies on the ageing of lithium-ion battery module under constant and monthly average ambient temperature. J. Energy Storage **113**, 115642 (2025). https://doi.org/10.1016/j.est.2025.115642
7. M. Moghadasi, M. Zarnoush, et al. Advancements and challenges in battery thermal management technologies for electric vehicles: A systematic navigation on the latest trends. Results in Engineering **27**, 105830 (2025). https://doi.org/10.1016/j.rineng.2025.105830
8. Jacob, R. D. Kumar, S. Varun, et al. Performance comparison of thermal control methods in EV batteries, in Proceedings of 6th International Conference on Electronics and Sustainable Communication Systems (ICESC), 67–73 (2025). https://doi.org/10.1109/ICESC65114.2025.11212368
9. H. Tomar, S. Singh, et al.Design and analysis of thermal management systems for an electric vehicle battery, in Proceedings of 1st International Conference on Advances in Computer Science, Electrical, Electronics, and Communication Technologies (CE2CT), 320–324 (2025). https://doi.org/10.1109/CE2CT64011.2025.10941560
10. K. R. Sree, S. Chowdary Polavarapu, B. et al.Thermal management system for electric vehicle batteries. in Proceedings of International Conference on Emerging Trends in Industry 4.0 Technologies (ICETI4T), 1–5 (2025). https://doi.org/10.1109/ICETI4T63625.2025.11132285
11. M. Elmahallawy, T. Elfouly, A. Alouani, A. M. Massoud, A comprehensive review of lithium-ion batteries modeling, and state of health and remaining useful lifetime prediction. IEEE Access **10**, 119040–119070 (2022). https://doi.org/10.1109/ACCESS.2022.3221137